Supporting Information

Design Bridging Solvation Structure by Recessive Solvents for High Energy Density Aqueous Zinc-Ion Batteries with 88% Depth of Discharge Zinc Rechargeability

Qingying Li,[a] Dan Luo,*[c] Qianyi Ma,[e] Zhuoyi Zheng,[b] Shibin Li,[b] Yihan Xie,[b] Linjiang Xue,[d] Meizhu Lin,[b] Yihang Nie,[a] Guo Feng,[a] Haozhen Dou,[c] Jiawen Chen,[a] Xin Wang,*[ad] Zhongwei Chen,*[c]

[a] South China Academy of Advanced Optoelectronics, South China Normal University, Guangzhou, 510006, China
Email: wangx@zwu.edu.cn
[b] School of Information and Optoelectronic Science and Engineering, South China Normal University, Guangzhou, 510006, China
[c] State Key Laboratory of Catalysis, Dalian Institute of Chemical Physics, Chinese Academy of Sciences, Dalian 116023, China
Email: luodan@dicp.ac.cn
zwchen@dicp.ac.cn
[d] Institute of Carbon Neutrality, Zhejiang Wanli University, Ningbo, 315100, China
[e] Department of Chemical Engineering, University of Waterloo, Waterloo, Ontario N2L 3G1, Canada

Experimental Section

Electrolyte configuration:

Zinc sulfate ($ZnSO_4$), zinc chloride ($ZnCl_2$), zinc nitrate [$Zn(NO_3)_2$], zinc acetate [$Zn(OAc)_2$], zinc trifluoro-methane-sulfonate [$Zn(OTF)_2$], and zinc bis-(trifluoro-methane-sulfonyl)-imide [$Zn(TFSI)_2$] were all purchased from Aladdin without further purification. The pure aqueous $Zn(OTF)_2$ electrolyte was prepared by dissolving 3M $Zn(OTF)_2$ in deionized water. Other electrolytes were prepared by dissolving the aforementioned zinc salts in a mixed solvent consisting of 30 vol% Hexafluoro-2-propanol (HFIP) and 70 vol% deionized water. Additionally, modified electrolytes were prepared by dissolving 3M $Zn(OTF)_2$ in mixed solvents with different volume ratios of HFIP to H_2O.

Synthesis of $V_2O_5 \cdot nH_2O$:

The $V_2O_5 \cdot nH_2O$ (VOH) were prepared by a facile hydrothermal method. Typically, 2 mmol (0.36 g) V_2O_5 was dissolved in 80 mL of deionized water under stirring for 30 min and transfer it into 100 mL PTFE liner. 2 mL of H_2O_2 was added into liner and stir for another 30 min and then hydrothermal react at 120°C for 6 h. The obtained product was directly freeze-dried for 96 h.

Electrolyte/Materials Characterization:

The Fourier-transform infrared (FT-IR) spectra and Raman spectra were employed to analyze the interaction between different components of the electrolyte. The FT-IR spectra were measured using Thermo-Fisher Scientific iS50 and Raman spectra were measured using the Renishaw inVia reflex Raman Microscope (Renishaw Co., Ltd., UK). Two-dimensional small-angle/wide-angle X-ray scattering (Xeuss 3.0, light source: high brightness micropaedic spot liquid GA target light source, wavelength 1.341Å, maximum power 250W) detected the presence of capsule-like nanoclusters inducted by bridging structure. NMR analysis was performed on a Varian 400MHz to further illustrate the chemical shift of H, F changes in the phase separating electrolyte. To minimize the impact on the samples, a coaxial double tube was utilized, with $CDCl_3$ in the inner tube and the electrolyte in the outer tube. The X-ray absorption spectra (XAS) including X-ray absorption near-edge structure (XANES) and extended X-ray absorption fine structure (EXAFS) of the samples at Zn K-edge (9659 eV) explores the coordination information of the Zn^{2+} inner solvation layer (Shanghai Synchrotron Radiation Facility, SSRF, BL11B). The Zn K-edge XANES data were recorded in fluorescence mode. Furthermore, the FT-IR spectra of –OH were employed to assess the variations of water contents at different states in different electrolytes.

Zn anode Characterization:

XPS is used to analysis the SEI composition in the Zn anode (Thermo-Fisher Scientific ESCALAB Xi, microfocus monochrome Al Kα X-ray light source: 20 μm ~ 900 μm continuously adjustable). Depth analysis of the SEI element components of the Zn anode SEI by TOF-SIMS (TOF. SIMS5-100). The morphology of the Zn anode surface is observed by SEM (Sigma 500).

Synchrotron 2D GIXRD measurement:

The Synchrotron 2D GIXRD were performed on VESPERS beamline at the Canadian Light Sources. The Zn anode after cycling were taken out from coin cell and washed by deionized water and ethanol. The beam size used for experiment is ~3×6 μm. The incident angle is 0.6° and 1.6°. The energy of X-ray beam used for

GIXRD is 11 keV. The beam diffracted from Zn anode was collected by a 2D area detector centered at 40° and located 120 mm away from the sample, which covers a 2θ angular range of 10° ~ 70°.

In-situ optical microscope:

Zn//Zn symmetric cell is fabricated in the custom-designed electrochemical cell to observe the stripping/plating process of Zn metal. The current density applied is 5 mA cm^{-2}.

Fabrication of symmetric/asymmetric cell:

For Zn//Zn symmetric cell, two pieces of Zn foils with a thickness of 50 μm (Φ15 mm) were used as two electrodes for symmetric cell. Different electrolytes were added into the CR2032-type coin cell with a piece of glass fiber (GF/D, Whatman) as separator. For Zn//Cu asymmetric battery, the same assembly process, the only difference being the replacement of one side of the Zn foil with a copper foil (Cu, 20 μm, Φ15 mm).

Fabrication of Zn//VOH full battery:

The cathode was prepared by mixing the active materials (VOH), conductive carbon (Super P), and PVDF in a weight ratio of 7:2:1 in NMP. Subsequently, the slurry is drop onto carbon cloth and dried overnight in vacuum oven at 60°C. The mass loading in the cathode is ~1.2 mg cm^{-2}. The electrode was cut into a circular shape (Φ=15 mm) as the cathode. Zinc foil (Φ15 mm, 50 μm thickness) is used directly as the anode after washing with ethanol and acetone, and the pure aqueous or hybrid 3M $Zn(OTF)_2$ as the electrolyte, glass fiber (GF/D, Whatman) as the separator in CR2032 coin cells. For the pouch cell, the cathode was prepared by mixing the active materials (VOH), conductive carbon (Super P), and PTFE in a weight ratio of 7:2:1. Then, the mixture was roll-pressed onto stainless steels mesh and dried at 60°C for 6 hours. The zinc foil (30 μm) and the cathode were cut into 6 cm × 9 cm sheets. The mass loading in the cathode is ~14.29 mg cm^{-2}.

Electrochemical Characterization:

The performances of Zn//Zn symmetric cells, Zn//Cu asymmetric cells, and Zn//VOH full cells were collected by battery test system (Neware BTS-4000). The linear scan voltammetry (LSV), Chronoamperometry (CA) and AC Impedance (EIS) are carried out utilizing an electrochemical workstation (CHI 760E Chenhua, Shanghai).

Theoretical Simulations

DFT calculations

All quantum chemical calculations were performed by applying the density functional theory (DFT) method with the B3LYP level and 6-311+G (d, p) basis set using Gaussian 09 program package. The structural optimization was determined by minimizing the energy without imposing molecular symmetry constraints. The binding energies of the Zn^{2+}, OTF^{-}, H_2O and HFIP were defined as the interaction between different molecule fragments. The binding energy E, was calculated according to the equation as follows:

$$E = E_{total} - E_X - E_Y$$

where E_{total} is the structure total energy, E_X and E_Y is the energy of different molecule fragments (X, Y = Zn^{2+}, OTF^{-}, H_2O and HFIP) according to the different structure configurations.

Molecular dynamics (MD) simulations:

Classic molecular dynamics simulations were carried out to give an atom-level insight of the structure of $Zn(OTF)_2$ in two kinds of solvation, one is consisted of water, the other is consisted of hexafluoro-isopropanol and water. The component and amount of two simulated system are listed in Table 1. Both the initial configurations of solvation systems were constructed through the software of PACKMOL1, all the molecules were randomly inserted in a cubic simulation box. The GROMOS54a7 force field2 was employed to describe the behavior of the molecules. The molecular force field is consisted of nonbonded and bonded interaction. The nonbonded interaction contains van deer Waals (vdW) and electrostatic interaction, which is described by the Equation 1 and Equation 2, respectively.

$$E_{LJ}\left(r_{ij}\right) = 4\varepsilon_{ij}\left(\left(\frac{\varepsilon_{ij}}{r_{ij}}\right)^{12} - \left(\frac{\varepsilon_{ij}}{r_{ij}}\right)^{6}\right)$$

$$E_c\left(r_{ij}\right) = \frac{q_i q_j}{4\pi\varepsilon_o\varepsilon_r r_{ij}}$$

For different kinds of atoms, the Lorentz-Berthelot mix rules were adopted for vdW interactions, which is following the Equation 3. The cutoff distance of vdW and electronic interactions was set to 1.2 nm, and the particle mesh Ewald (PME) method was employed to calculate long-range electrostatic interactions.

$$\sigma_{ij} = \frac{1}{2}\left(\sigma_{ii} + \sigma_{jj}\right); \varepsilon_{ij} = \left(\varepsilon_{ii} * \varepsilon_{jj}\right)^{1/2}$$

The initial configuration setup for each simulation system are as follows:

Electrolyte model	Zn^{2+}	OTF^-	HFIP	H_2O
System 1	200	400	393	3888
System 2	100	200	/	2780

For each simulation, an energy minimization was firstly employed to relax the simulation box. Then, an isothermal-isobaric (NPT) ensemble with a 1.0 fs time step is employed to optimized the simulation box. The pressure of both systems is set to 1.0 atm, which is kept via the Parrinello-Rahman barostat. System 1 and 2 was simulated under 298.15 K. The temperature is kept via the Nose-Hoover thermostat barostat. The NPT optimization time was set to 10.0 ns, which is enough long to obtain a stable box size. Following the NPT simulation, a canonical (NVT) ensemble with 20.0 ns was performed to furtherly optimize the simulation box, the time step is set to 2.0 fs. At last, another 10.0 ns NVT simulation was performed to collect the trajectory coordinates of molecules with a storage frequency of 100 steps. The time step of NVT simulation was set to 1.0 fs. In all the MD simulation, the motion of atoms was described by classical Newton's equation, which was solved using the velocity-Verlet algorithm. All simulations were performed using the GROMACS 2019.5 package3.

Finite Element Analysis (FEA) methods：

The electric field and current density distributions were simulated and calculated by COMSOL software and compared for two different cases, conventional aqueous $Zn(OTF)_2$ and nano-capsule electrolytes (NCEs). The detailed parameters are given below:

Electrolyte model	$Zn(OTF)_2$	NCEs
Model size	9 μm * 8.5 μm	9 μm * 8.5 μm
Surface raised radius	1 μm	1 μm
Cluster adsorption layer	/	0.1 μm
Metal Zinc conductivity	$1.67 * 10^7$ S/m	$1.67 * 10^7$ S/m
Electrolyte conductivity	45 mS/cm	34 mS/cm
Cluster conductivity	/	$1.85 * 10^{-7}$ mS/cm
Upper boundary potential	70 mV	110 mV
Lower boundary potential	0	0

Results and Discussion

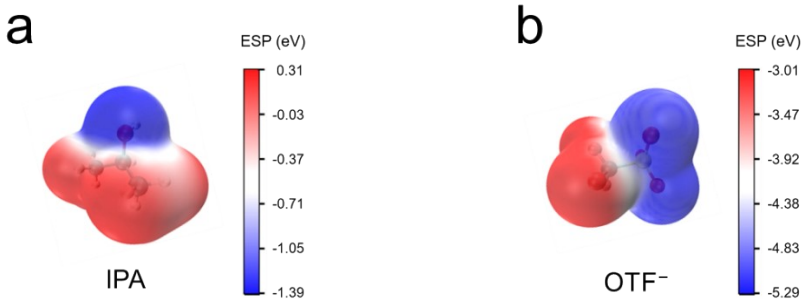

Figure S1. Electrostatic potential maps of (a) isopropanol (IPA) and (b) trifluoro-methane-sulfonic acid anions (OTF^-).

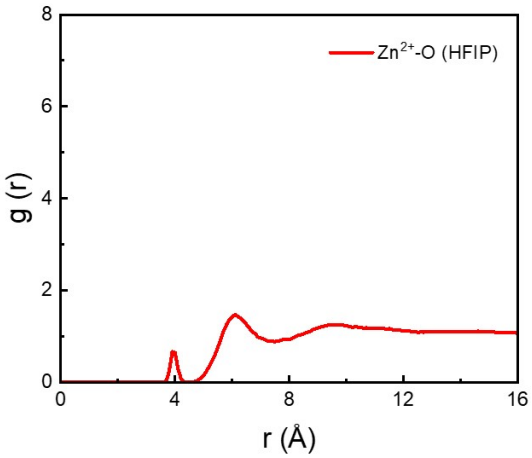

Figure S2. Radial distribution function (RDF) of Zn-HFIP coordination in $Zn(OTF)_2$ electrolyte at 298.15 K in a mixed solution of 30% HFIP, 70% H_2O.

Since the electrostatic potential distribution of HFIP exhibits $|ESP_{min}| < ESP_{max}$, it is unable to show an orientation preference for coordination with Zn^{2+} like normal alcohol molecules. Therefore, no coordination peak of Zn^{2+} with O in HFIP appears in the RDF results of MD simulations, especially at 2Å.

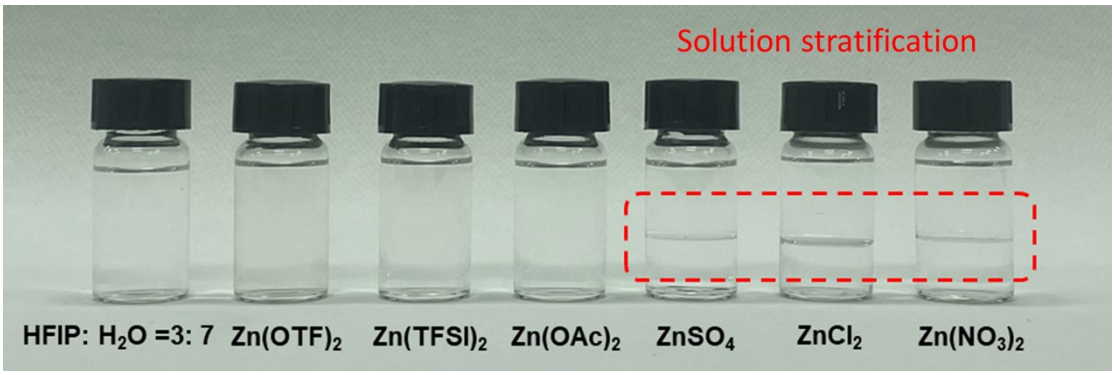

Figure S3. Pictures of different zinc salts after adding to a mixed solution of 30 vol% HFIP and 70 vol% H_2O.

Since SO_4^{2-}, Cl^-, and NO_3^- all lack polar groups, upon addition of the zinc salt to the mixed solution, the anion preferentially binds to the extremely positively charged HFIP, weakening or even eliminating the polarity of the HFIP, which results in an obvious stratification phenomenon of the HFIP and H_2O.

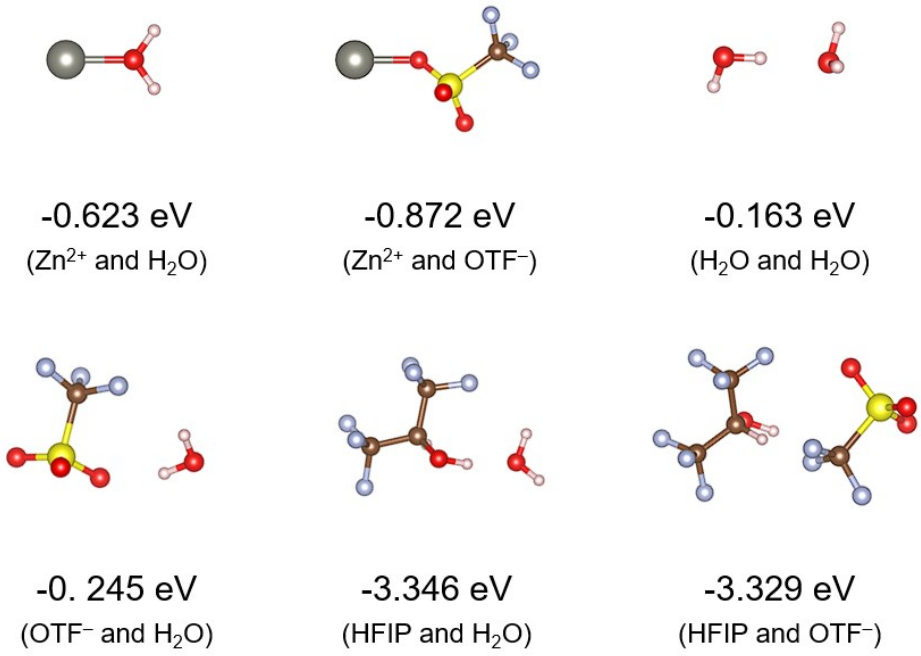

Figure S4. Binding energy between different components in electrolytes.

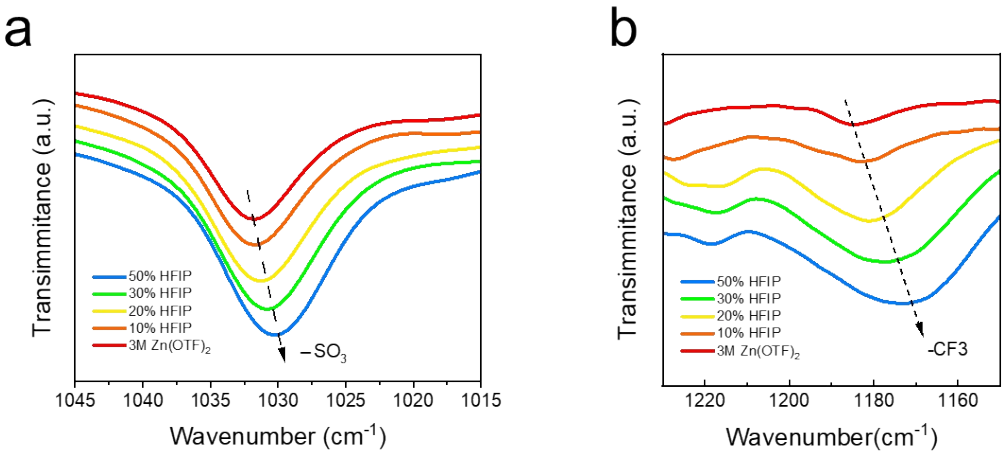

Figure S5. The FT-IR spectra of $-SO_3$ and $-CF_3$ groups in pure aqueous $Zn(OTF)_2$ solution and in mixed solutions with different volumes of HFIP.

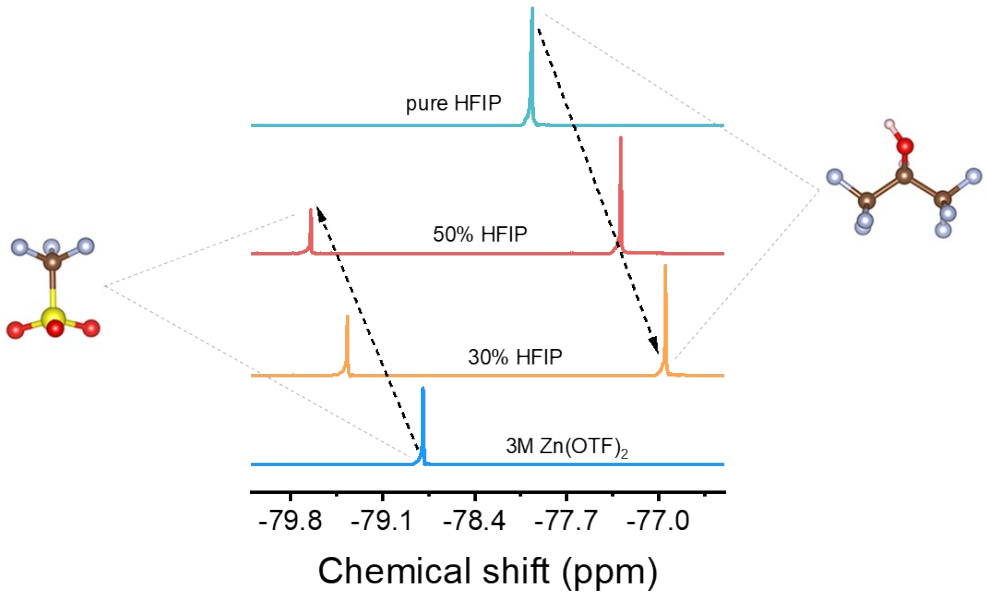

Figure S6. ^{13}F NMR in pure HFIP, pure $Zn(OTF)_2$ and different ratios of hybrid electrolyte.

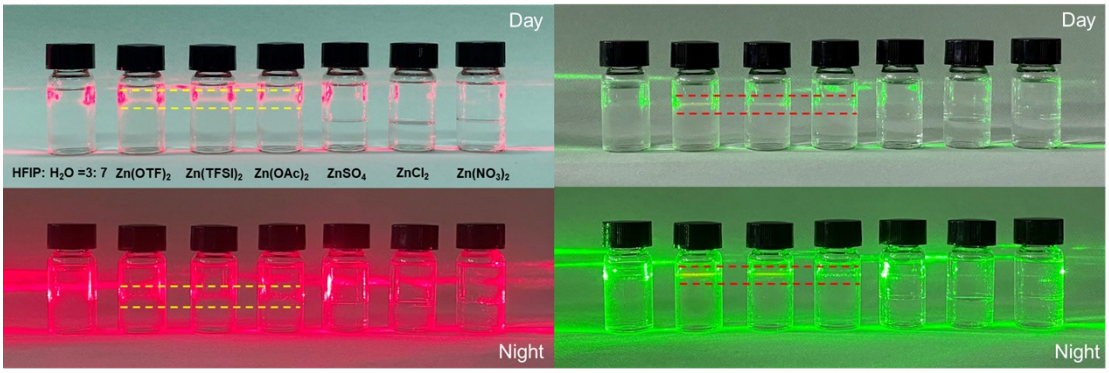

Figure S7. Tyndall effect of different colors (red and green) of laser in different zinc salt solutions.

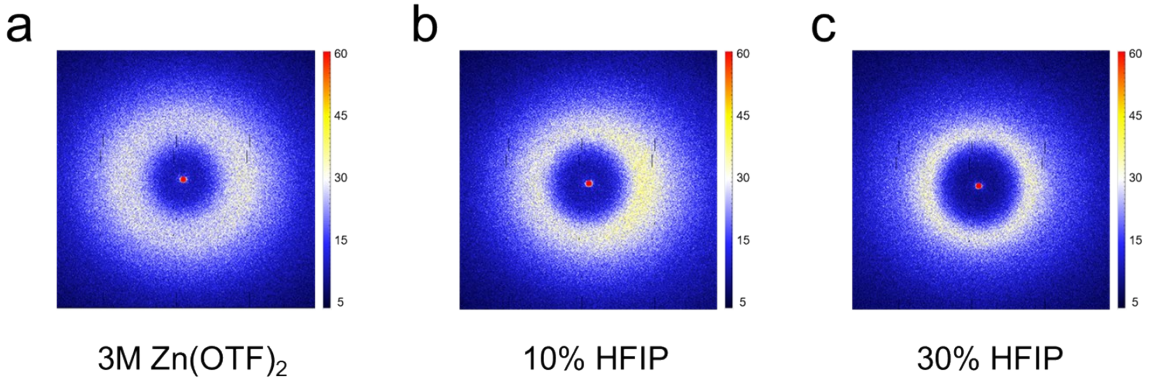

Figure S8. 2D SAXS for (a) 3M $Zn(OTF)_2$; (b) 10% HFIP; (c) 30% HFIP.

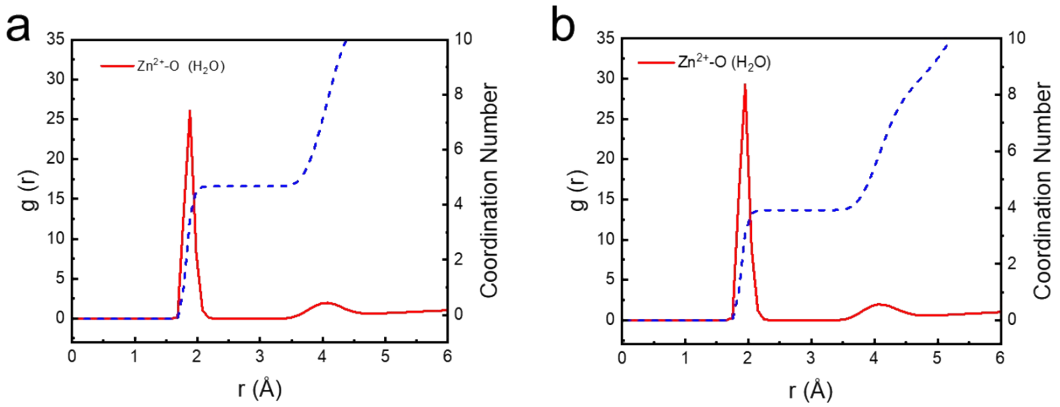

Figure S9. RDF of Zn-O (Water) coordination in (a) pure aqueous $Zn(OTF)_2$ electrolyte and (b) hybrid electrolyte (30% HFIP, 70% H_2O) at 298.15 K.

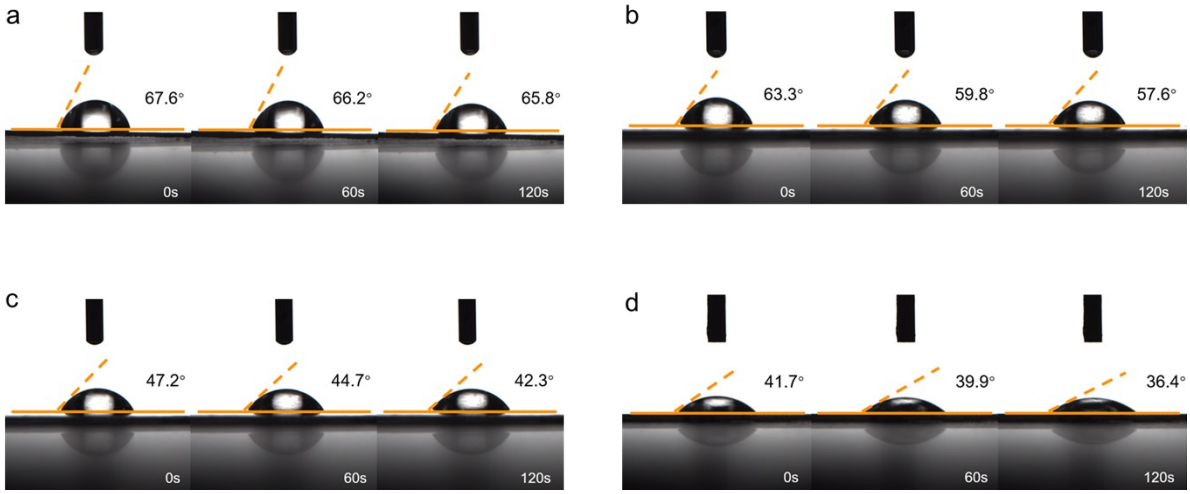

Figure S10. Contract angle for the (a)3M $Zn(OTF)_2$; (b)10%; (c)30%; (d)50% HFIP hybrid electrolyte on zinc plate.

Contact angle tests were performed for $Zn(OTF)_2$ and mixed electrolytes with different HFIP ratios and the results were recorded at 0s, 60s and 120s. With the increase of HFIP percentage, the contact angle of initial state continuously becomes smaller and the dynamic wettability of the interface is improved in the time from 0 to 120s, which is favorable for the stable interfacial transfer.

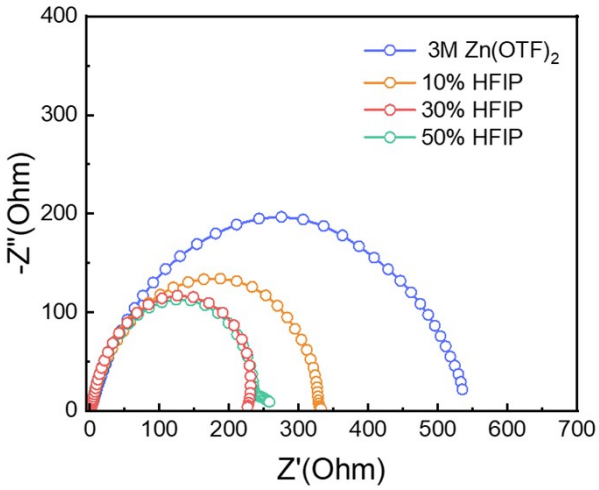

Figure S11. EIS spectra for different percentage of HFIP hybrid electrolyte from symmetric cell.

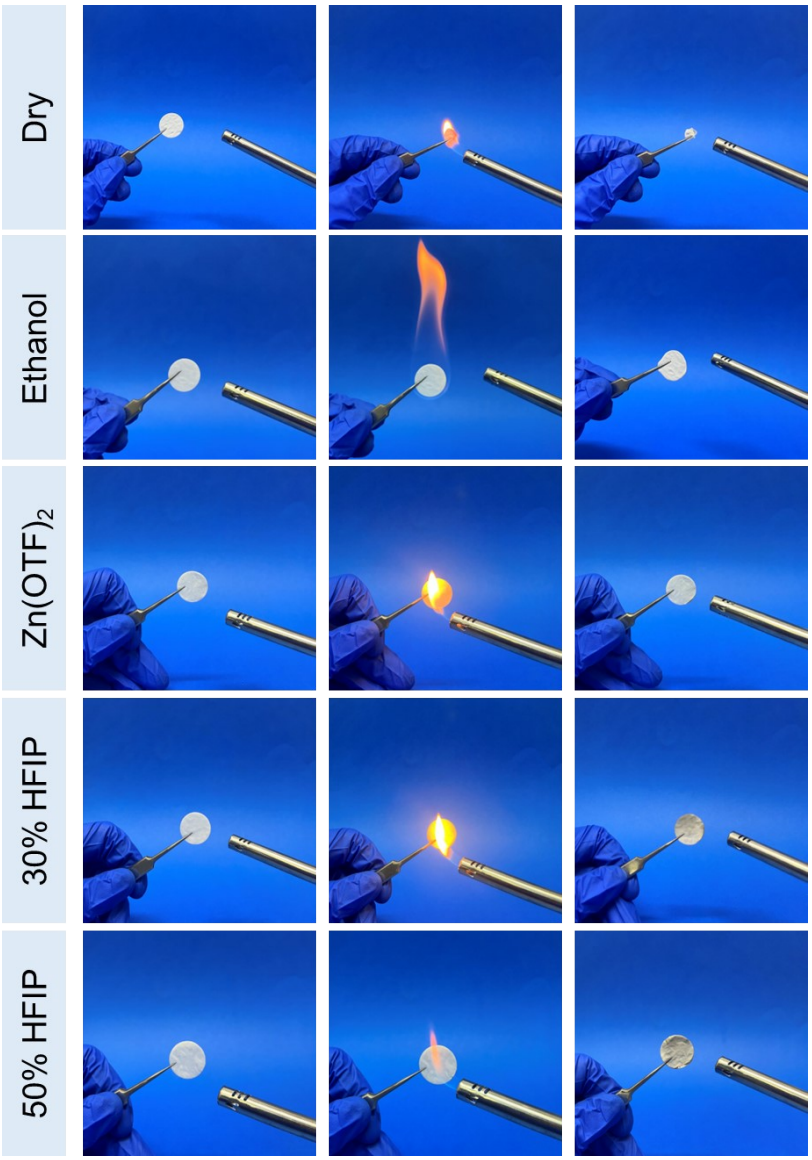

Figure S12. Flammability tests of electrolytes.

In addition, flammability tests of the electrolyte were carried out by directly igniting a glass fiber separator soaked in the electrolyte to evaluate its safety. The unsoaked dry glass fiber shrank immediately. The glass fiber soaked in conventional organic electrolyte such as ethanol are quickly ignited, and the glass fibers shrank slightly after the fire was extinguished. However, glass fibers soaked in hybrid electrolytes with HFIP content of 30% and 50%, failed to ignite. Therefore, the introduction of HFIP has not weakened the safety of the electrolyte, and it still has high reliability in battery applications.

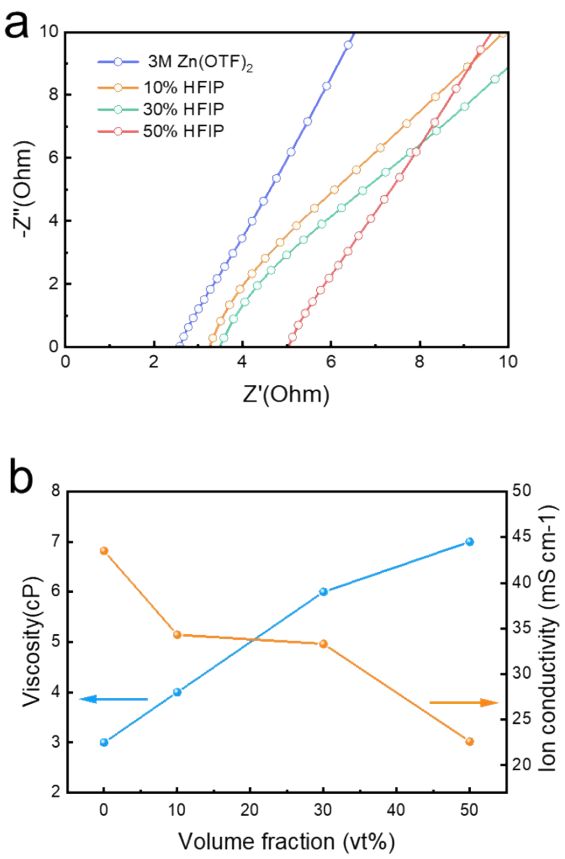

Figure S13. (a) Ion transport EIS for different percentage of HFIP,

(b) Viscosity and ion conductivity for different percentage of HFIP hybrid electrolyte.

The ionic conductivity of the electrolyte can be calculated via the following equation: $\sigma = {}^{L}\!/_{R_b S}$, in which

L is the distance between the two electrodes (2 mm), *S* is the contact area (1.767 cm^2) and R_b is the bulk resistance.

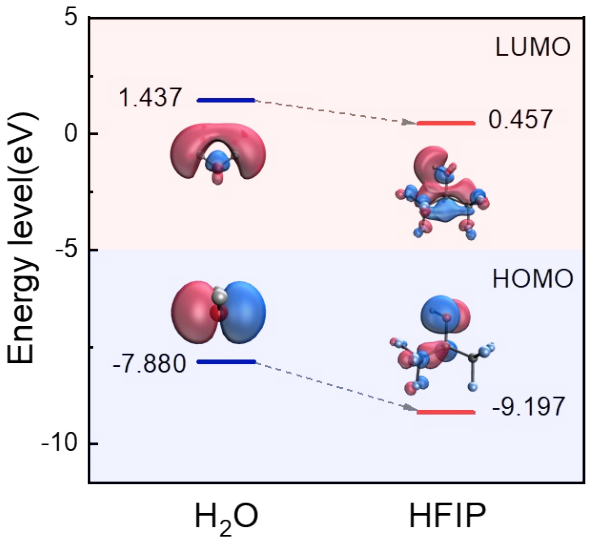

Figure S14. Calculated HOMO/LUMO Energy level of H_2O and HFIP molecule.

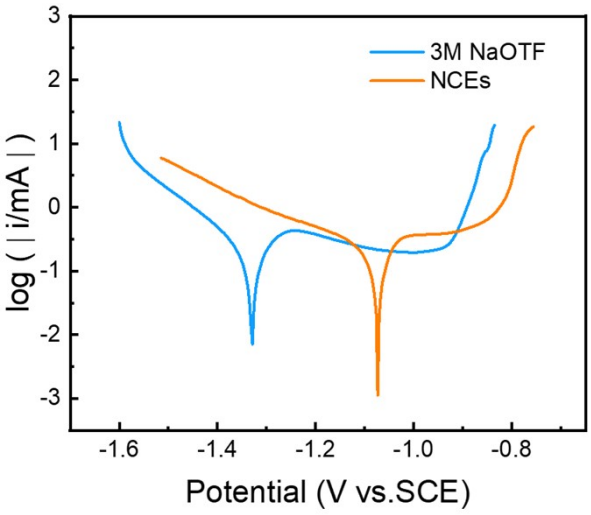

Figure S15. Tafel curves of Ti electrode in 3M NaOTF and NCEs.

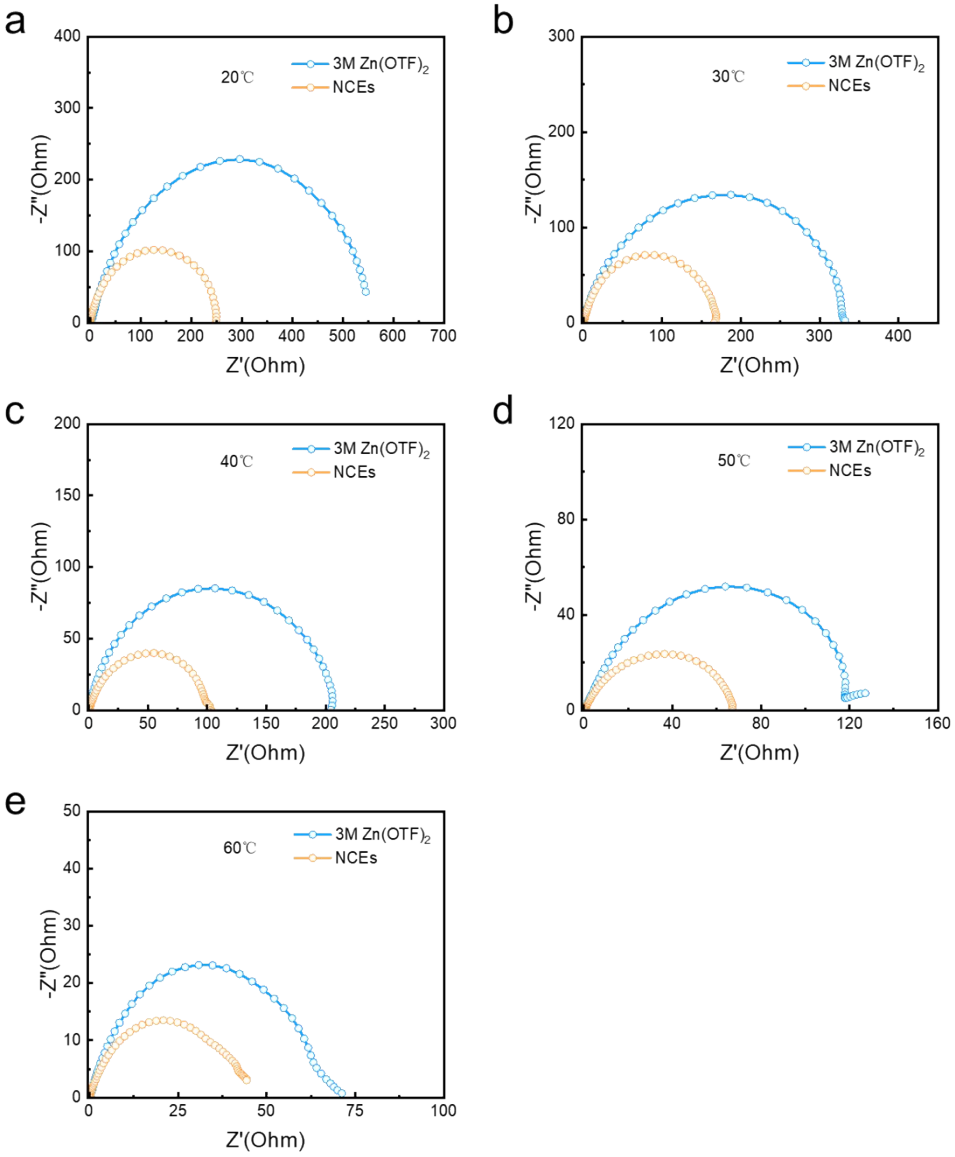

Figure S16. EIS spectra for different temperatures.

The Arrhenius activation energy (Ea) was calculated according to the following equation: $1/R_{ct} = Aexp\left(-E_a/RT\right)$, where R_{ct} is the interfacial charge transfer impedance, A and R are the frequency factor and gas constant, T indicates the absolute temperature. By taking the natural logarithm on both sides of the equation we can get $\ln\left(1/R_{ct}\right) = -E_a/RT + \ln A$, and then we can use the slopes obtained from the ln($1/R_{ct}$) and 1000/T linear fits to determine Ea.

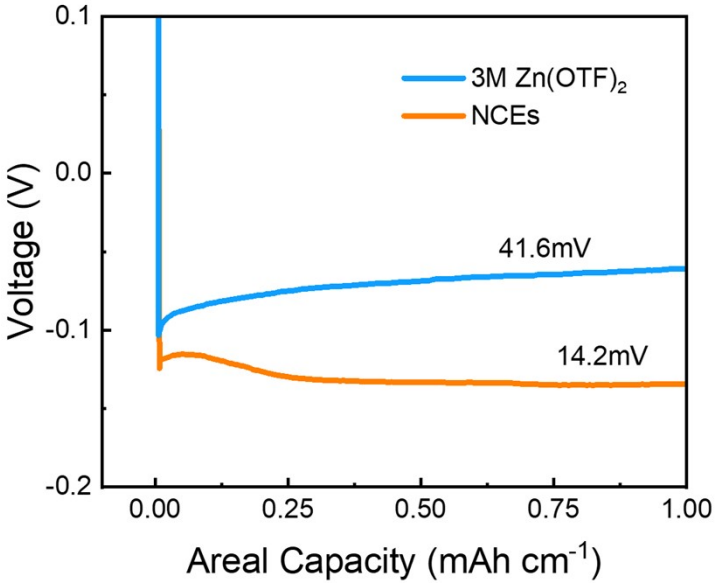

Figure S17. Overpotential of Zn deposition on the bare Cu in NCEs and aqueous 3M $Zn(OTF)_2$ at 25 ℃.

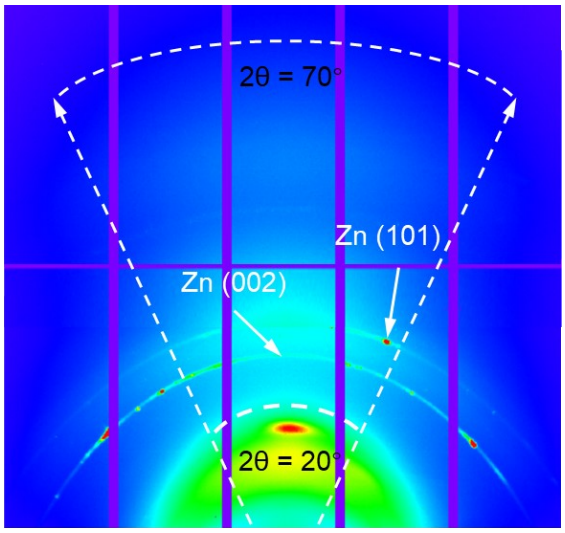

Figure S18. The GIXRD pattern of initial zinc metal.

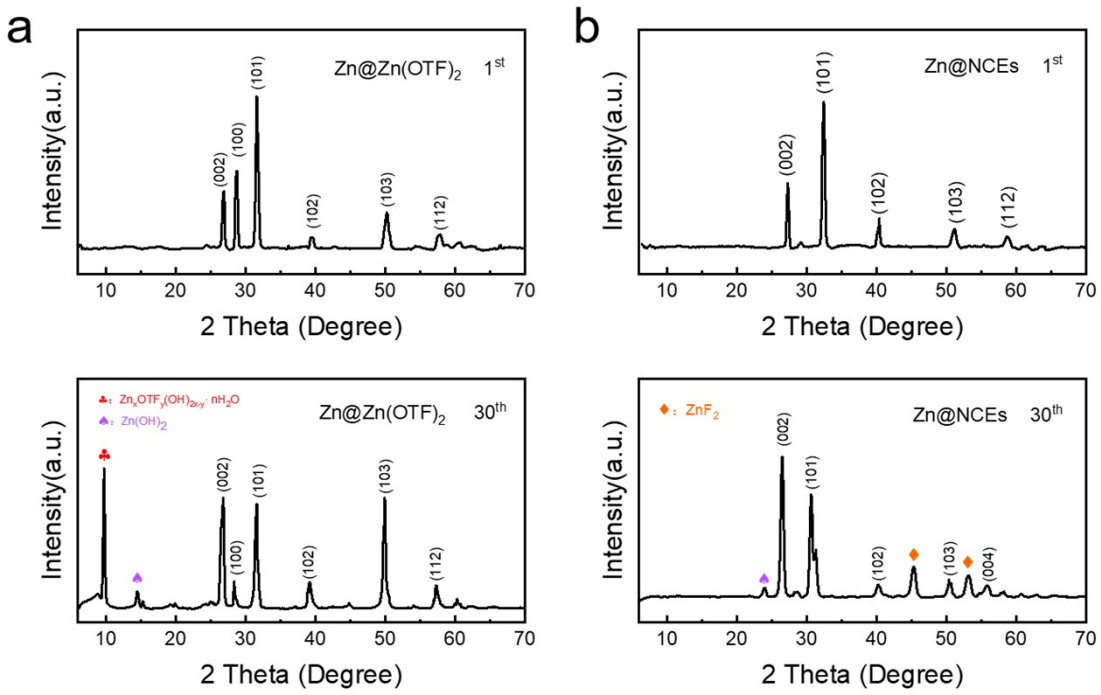

Figure S19. Corresponding integration curves of 2D GIXRD for Zn anode in (a) $Zn@Zn(OTF)_2$ and (b) Zn@NCEs after 1st and 30th stripping/plating process (current density of 1 mA cm^{-2} with a capacity of 1 mAh cm^{-2}).

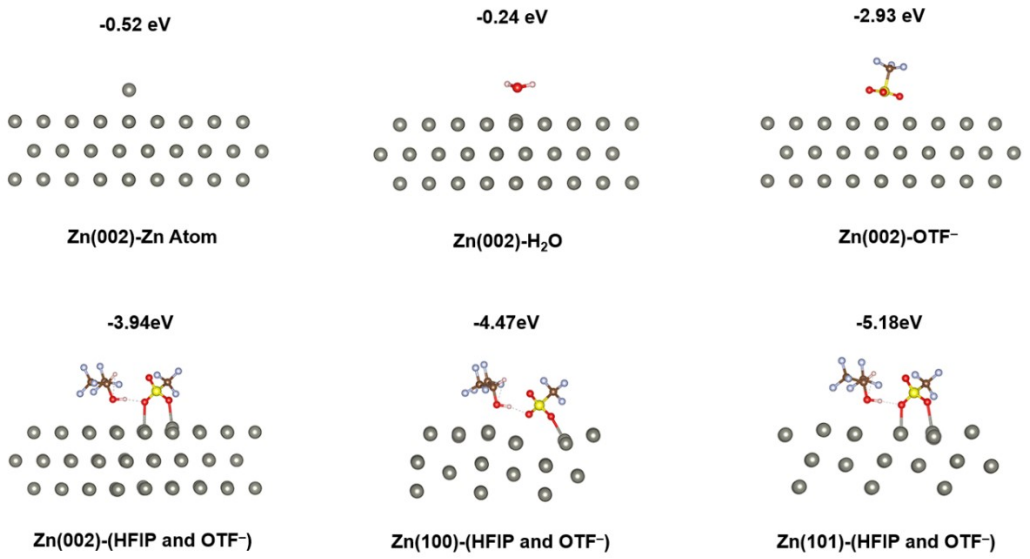

Figure S20. Schematic diagram of the adsorption of various components of the NCEs on different crystal surfaces.

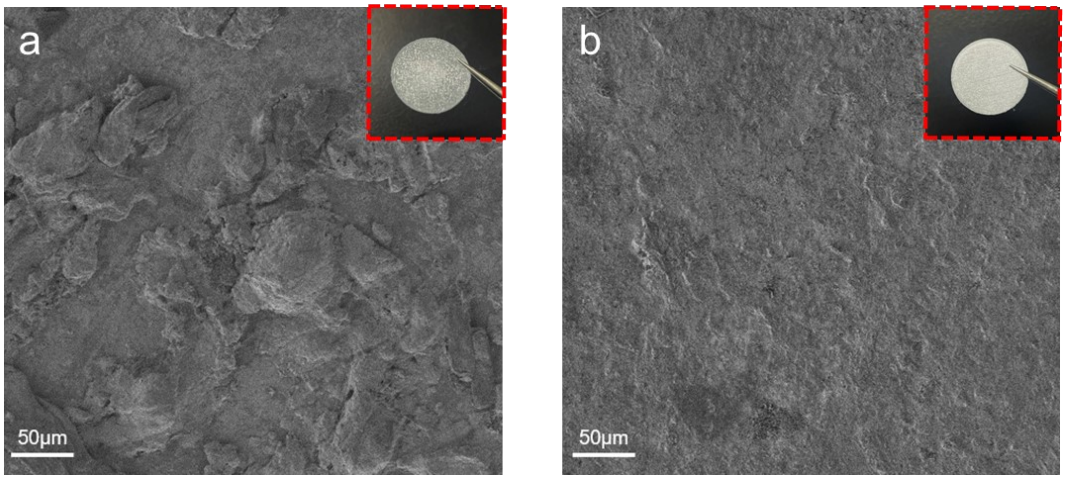

Figure S21. SEM image and optical photograph of Zn anode in (a) $Zn(OTF)_2$ and (b) NCEs after 30th stripping/plating process.

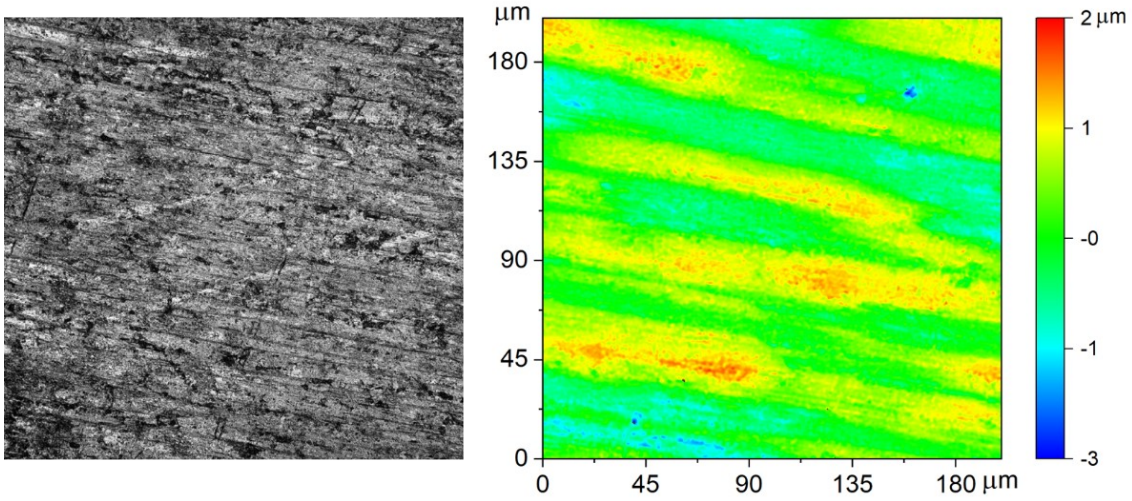

Figure S22. 3D height images for the original Zn anode surface.

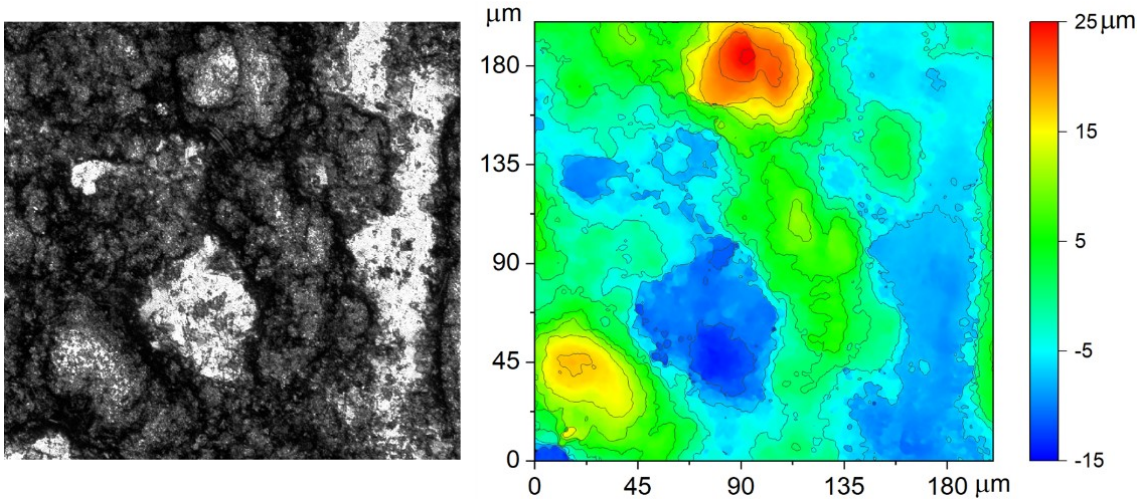

Figure S23. Surface and 3D height images for Zn@Zn(OTF)$_2$ after 30th stripping/plating process.

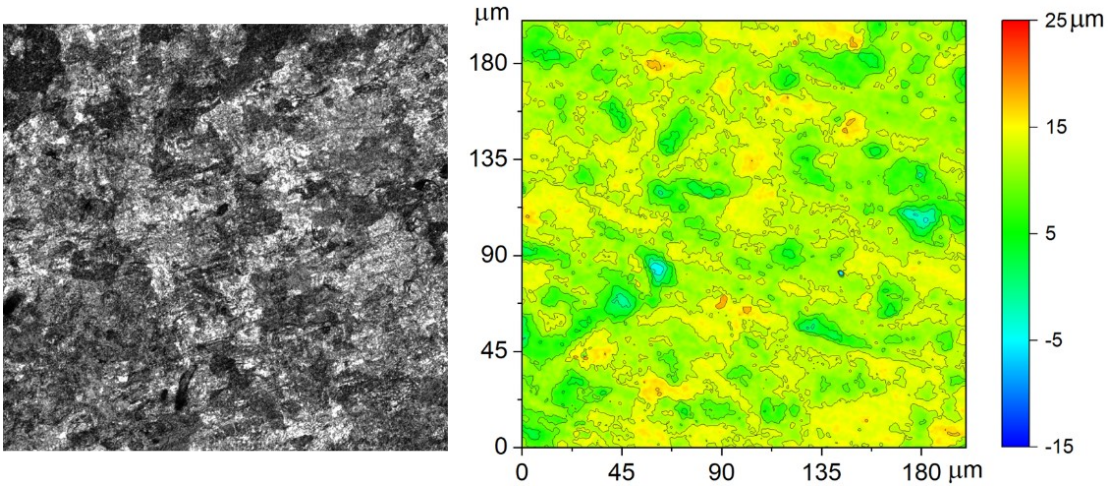

Figure S24. Surface and 3D height images for Zn@NCEs after 30th stripping/plating process.

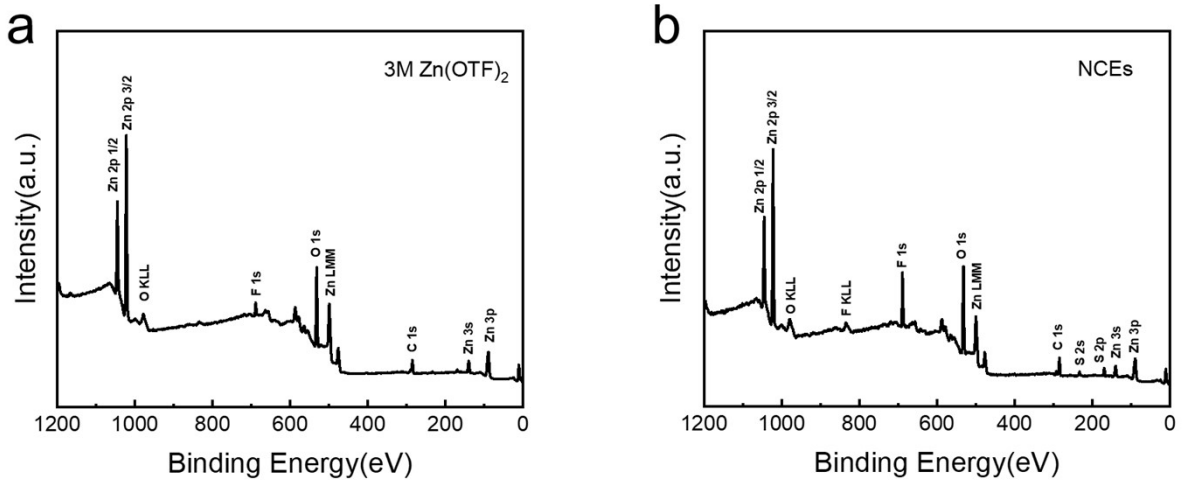

Figure S25. XPS survey spectra of (a) Zn electrode cycled in 3M $Zn(OTF)_2$ for 30 plating/stripping cycles and (b) the NCEs.

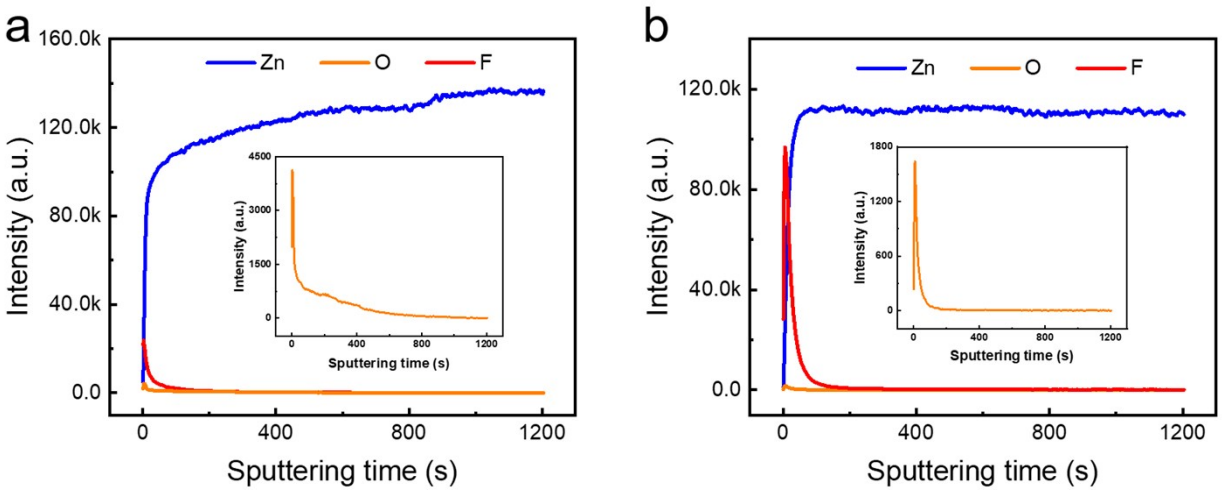

Figure S26. 1D curve of the element distribution of TOF-SIMS with the sputter time for Zn anode cycled in the (a) 3M $Zn(OTF)_2$ electrolyte and (b) NCEs.

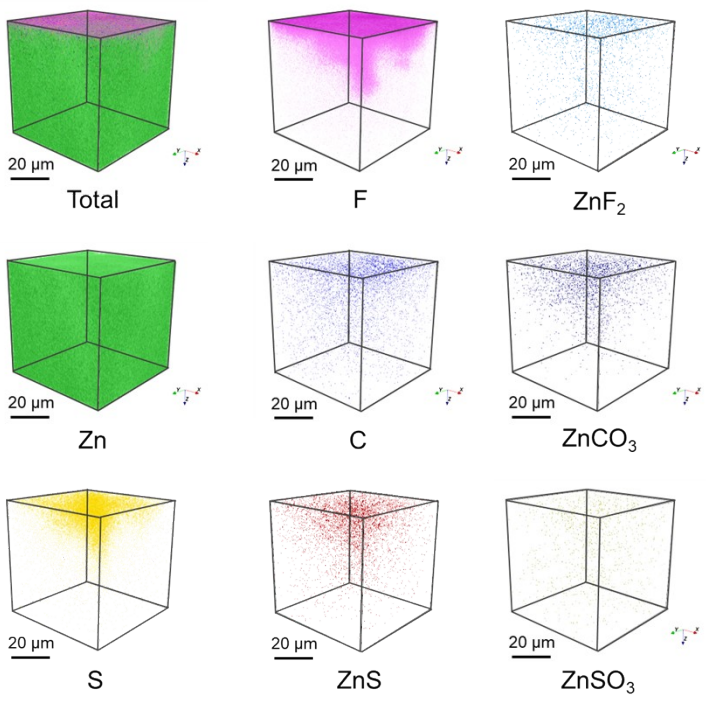

Figure S27. TOF-SIMS 3D reconstruction results of each component after deep sputtering of zinc plates after cycling in aqueous $Zn(OTF)_2$ electrolyte.

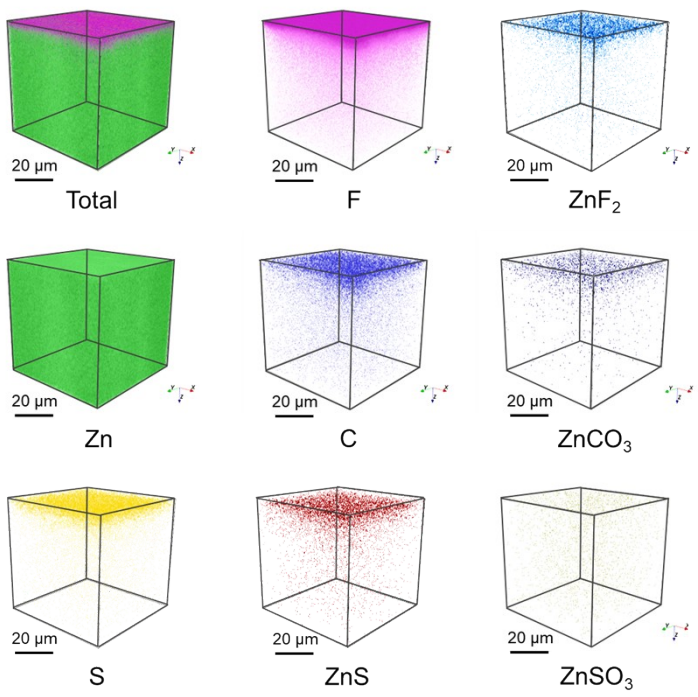

Figure S28. TOF-SIMS 3D reconstruction results of each component after deep sputtering of zinc plates after cycling in NCEs.

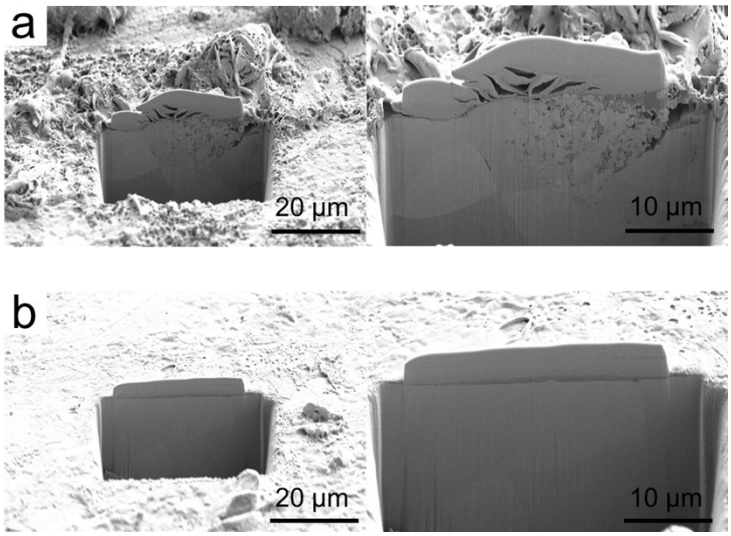

Figure S29. FIB-SEM images of Zn anodes in $Zn(OTF)_2$ and NCEs after 30th stripping/plating process at 1 mA cm^{-2} and 1 mAh cm^{-2}.

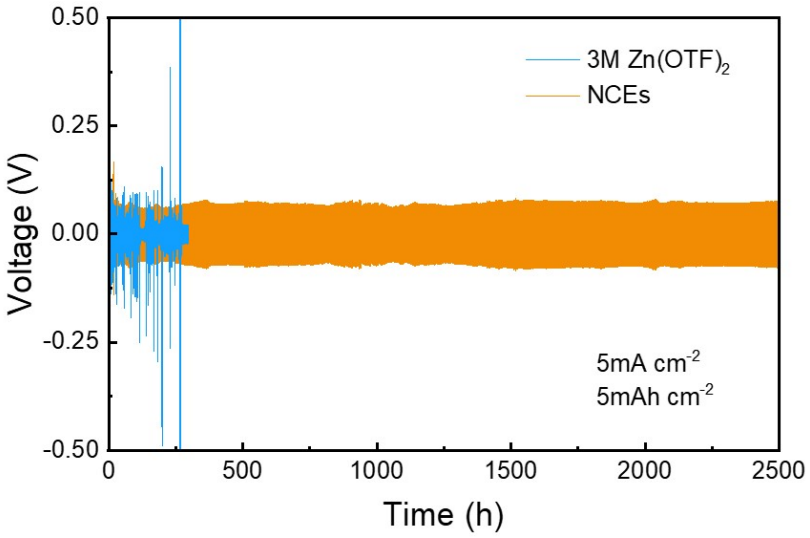

Figure S30. Zn//Zn symmetric cell with current density 5 mA cm^{-2} and areal capacity density of 5 mAh cm^{-2}.

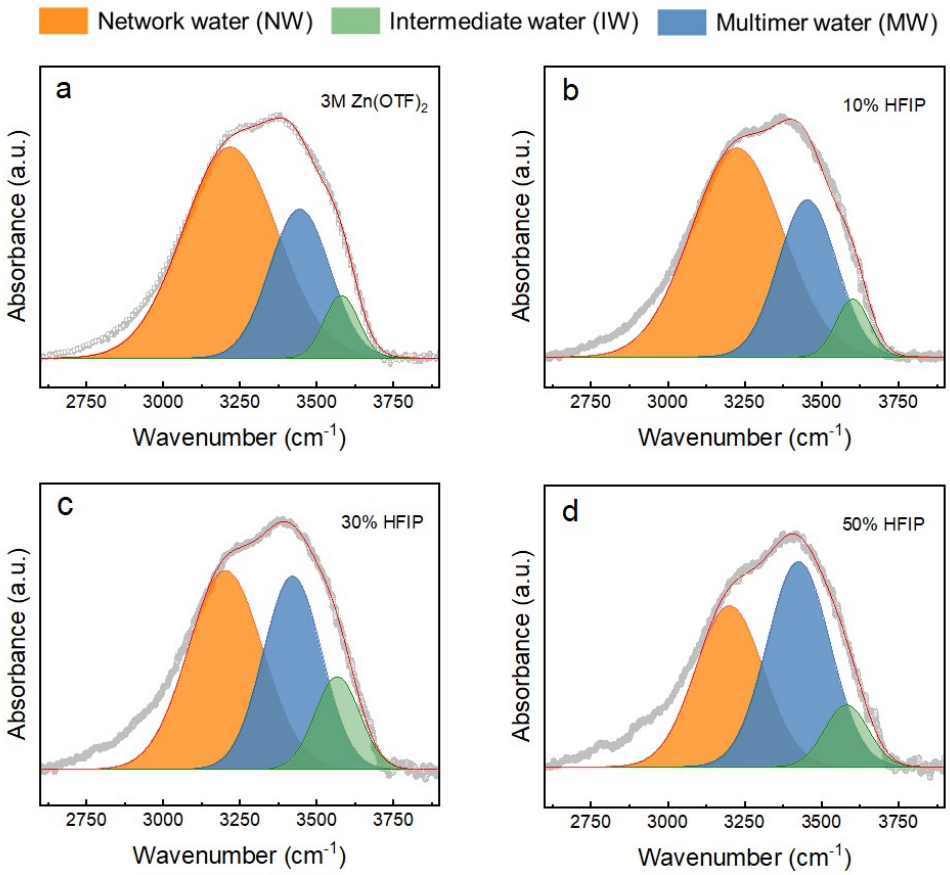

Figure S31. FT-IR spectra of (a) 3M $Zn(OTF)_2$; (b) 10%; (c) 30%; and (d) 50% HFIP hybrid electrolytes with typically fitted curves representing three states of water molecules: NW, IW, and MW.

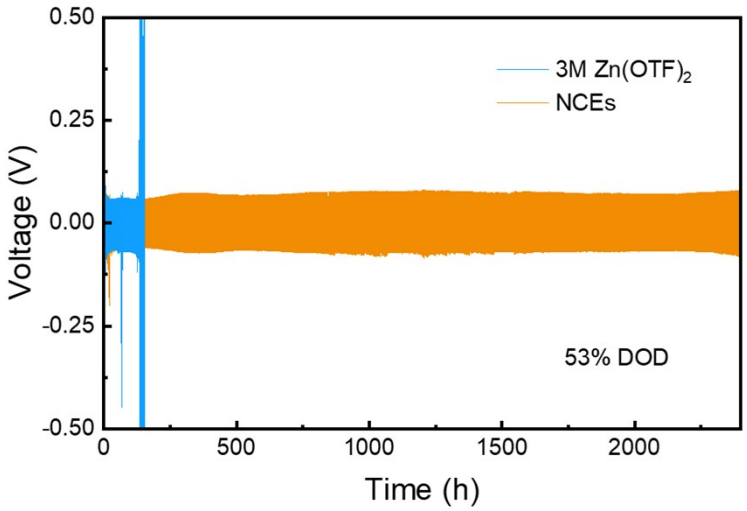

Figure S32. Zn//Zn symmetric cell with 53% depth of discharge.

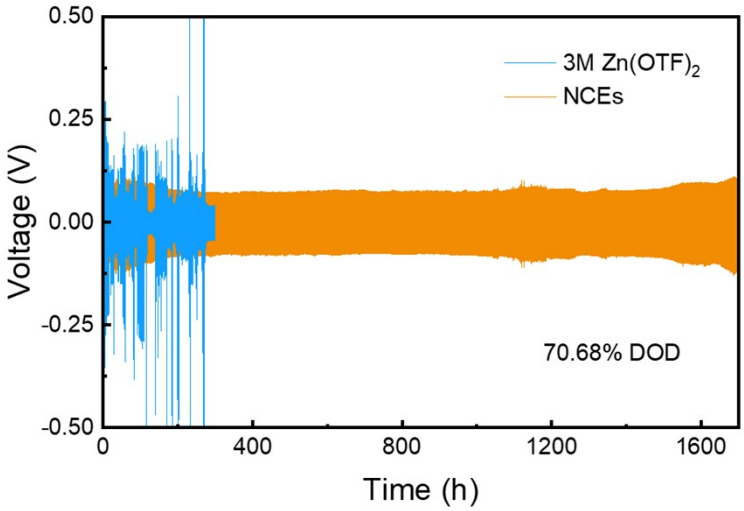

Figure S33. Zn//Zn symmetric cell with 70.68% depth of discharge.

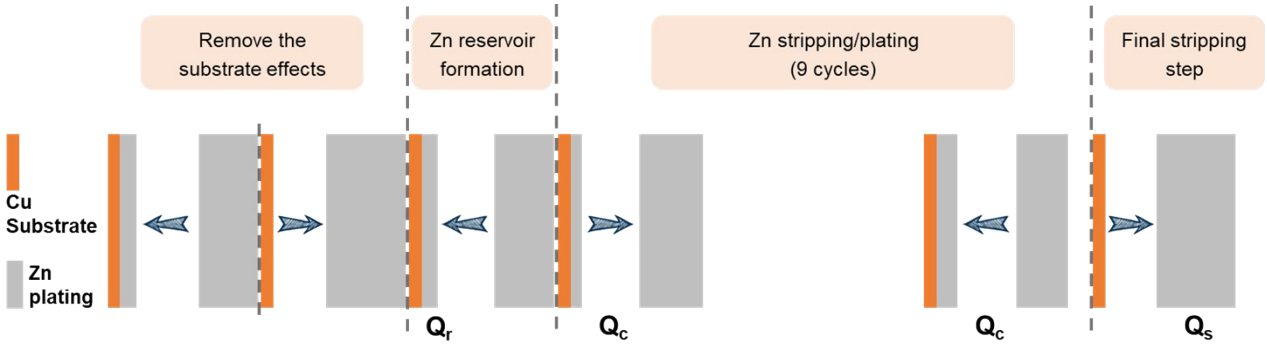

Figure S34. Proposed galvanostatic cycling protocol for evaluating Zn stripping/plating CE.

First, the Cu cathode undergoes an initial Zn plating/stripping process, which can effectively remove the substrate effects between Zn and Cu (lattice mismatch, alloying, and phase interface effects). Subsequently, a “zinc reservoir” of fixed capacity (Q_r) is pre-deposited on Cu as a limited high quality zinc source, and the stored Zn is cycled for nine times by fixed capacity Q_c ($Q_c < Q_r$). Finally, it is stripped to the preset cutoff voltage (0.5 V vs Zn/Zn^{2+}), and all active Zn^{2+} should be stripped (Q_s). CE is calculated according to the follow formula:

$$CE = \frac{9Q_c + Q_s}{9Q_c + Q_r}$$

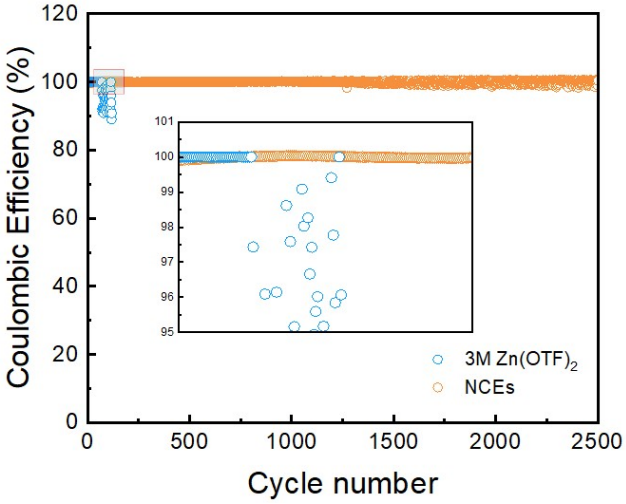

Figure S35. Coulombic efficiency of Zn plating/stripping at 1 mA cm^{-2}.

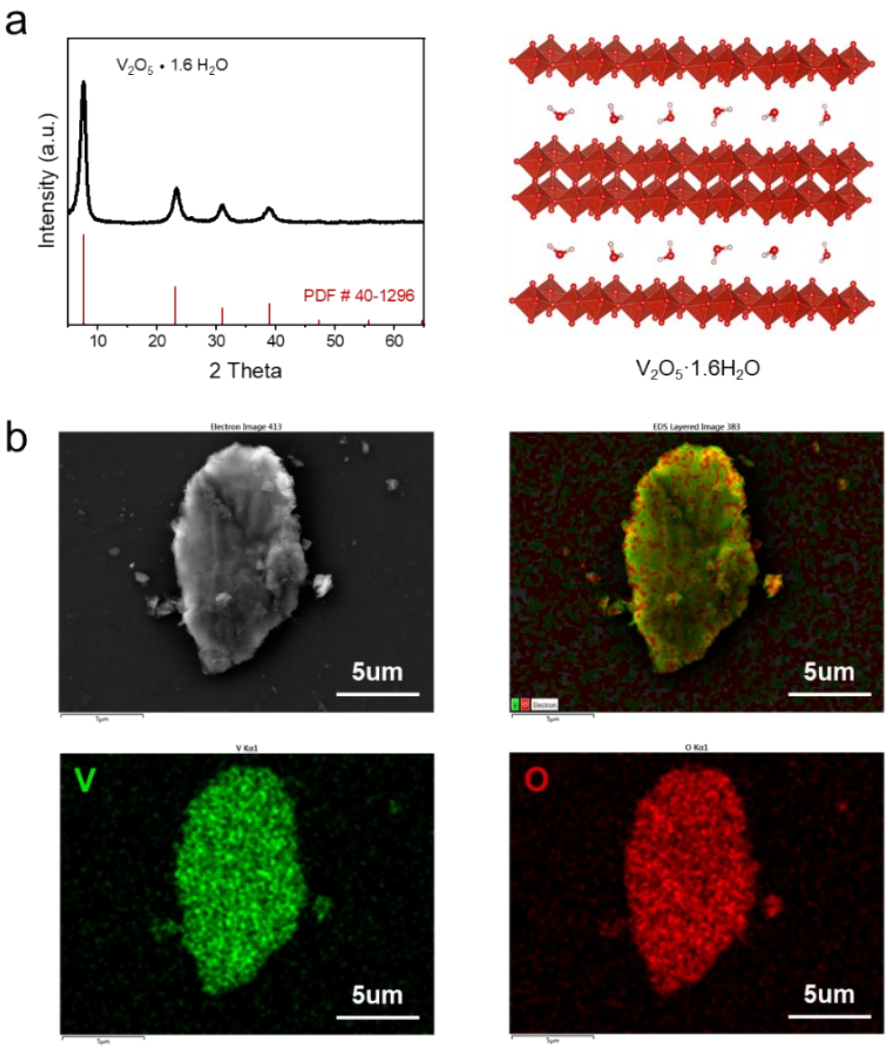

Figure S36. (a) XRD pattern (with crystal structure); (b) SEM image and elemental distribution of $V_2O_5 \cdot 1.6H_2O$.

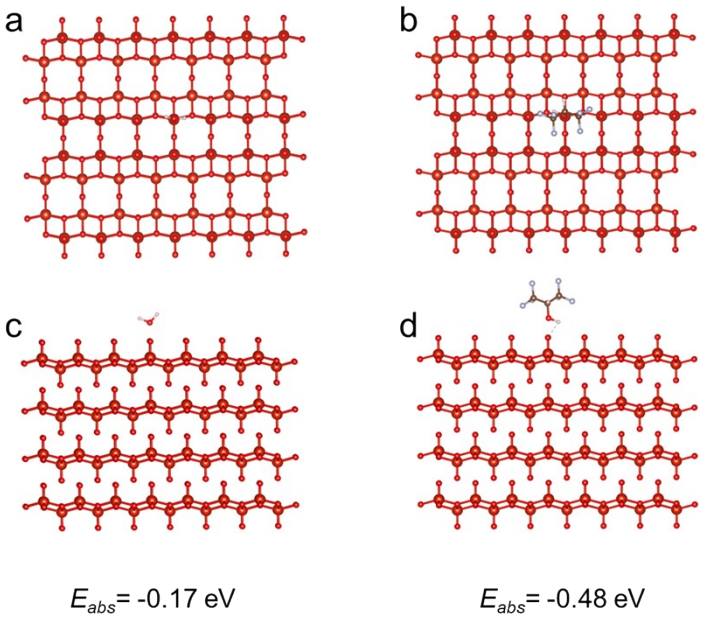

Figure S37. Adsorption energies of (a, c) H_2O and (b, d) HFIP on the VOH (001) crystal plane.

Figure S38. Cathode soaking tests.

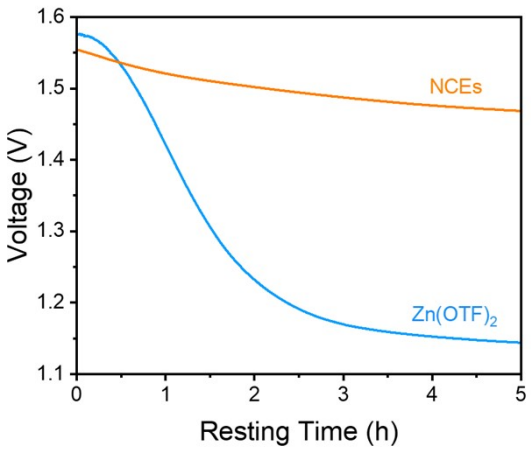

Figure S39. Voltage drop curves of Zn//VOH full cells resting for 5h.

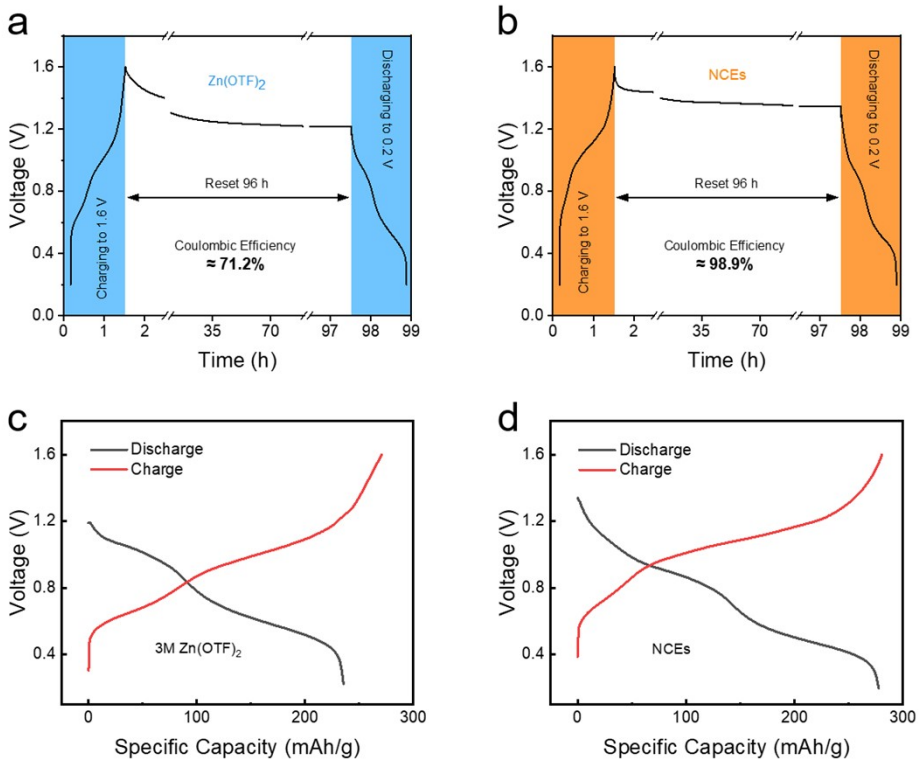

Figure S40. Self-discharge test of Zn//VOH full cell resting for 96h.

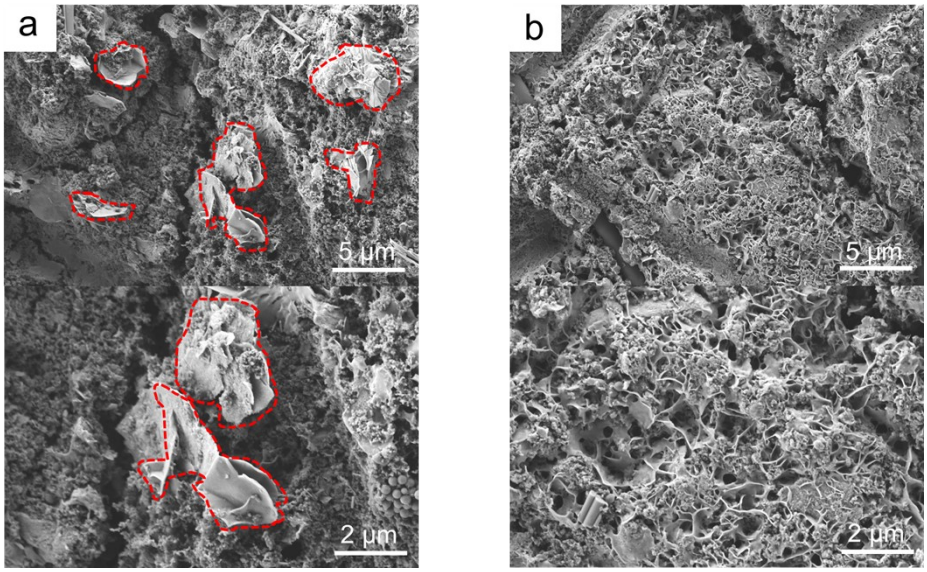

Figure S41. SEM images of VOH cathode for (a) 30 and (b) 100 cycles in aqueous $Zn(OTF)_2$.

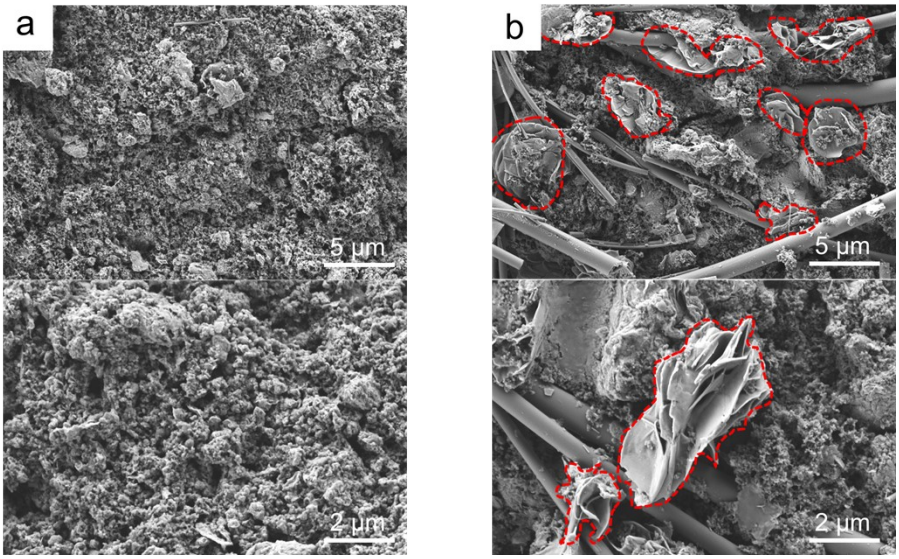

Figure S42. SEM images of VOH cathode for (a) 30 and (b) 100 cycles in NCEs.

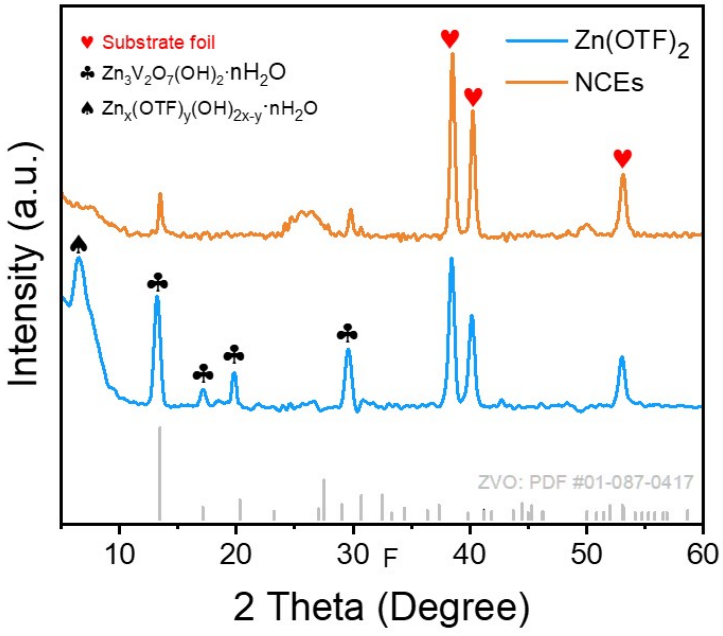

Figure S43. XRD of VOH cathode after 100 cycles in $Zn(OTF)_2$ and NCEs.

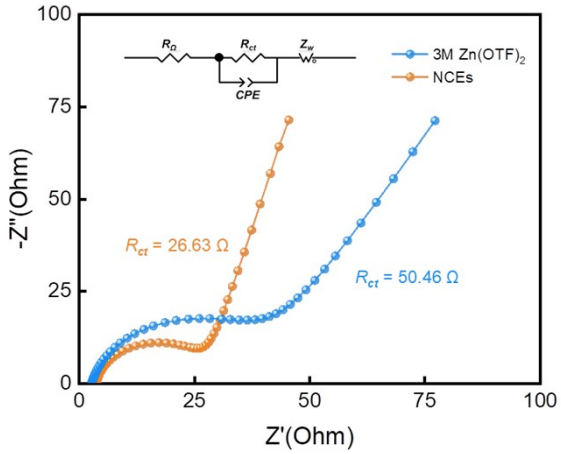

Figure S44. EIS fitting curves after 100 cycles of Zn//VOH full cell.

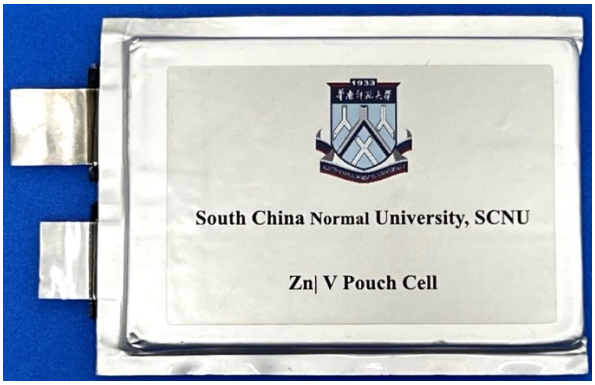

Figure S45. Photograph of stacked Zn//VOH pouch cell.

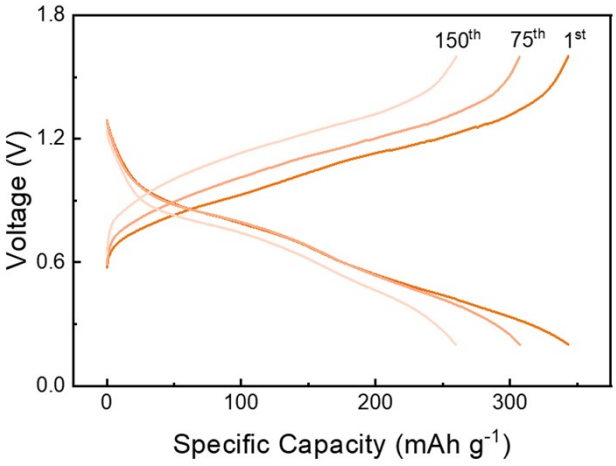

Figure S46. GCD curves of Zn//VOH pouch cell with NCEs.

Table S1. Comparison of the electrochemical performances of Zn symmetric cells reported in recent years.

Component	Max current density ($mA\ cm^{-2}$)	Cumulative capacity density ($Ah\ cm^{-2}$)	Ref.
NCEs	50 $mA\ cm^{-2}$	170 $Ah\ cm^{-2}$	this work
trifluoroacetamide (TFA) additive	10 $mA\ cm^{-2}$	10 $Ah\ cm^{-2}$	[1]
eutectic solvation shell 2-propanol	15 $mA\ cm^{-2}$	7.5 $Ah\ cm^{-2}$	[2]
DMTFA, DMF co-solvent	20 $mA\ cm^{-2}$	84 $Ah\ cm^{-2}$	[3]
polyzwitterion protective layer	40 $mA\ cm^{-2}$	40 $Ah\ cm^{-2}$	[4]
Manual SEI $Zn_3(BO_3)_2$	60 $mA\ cm^{-2}$	24 $Ah\ cm^{-2}$	[5]
in situ SEI $LiB(C_2O_4)_2$	100 $mA\ cm^{-2}$	38 $Ah\ cm^{-2}$	[6]

Table S2. Comparison of the DOD (depth of discharge) and stability of Zn anode reported in recent years.

Component	DOD (%)	Time (hours)	Ref.
NCEs	88.07%	1600 hours	this work
(002)-textured Zn electrodeposition on textureless substrates	45.5%	220 hours	[7]
fibroin hydrogel electrolyte, (SFPAM-Zr)	57%	230 hours	[8]
DMC and $LiNO_3$ additive	65%	1500 hours	[9]
polyzwitterion protective layer (PZIL)	74.5%	380 hours	[4]
$La(NO_3)_3$ additive	80%	160 hours	[10]
polymer additive by copolymerizing MPC and NAGA	90%	420 hours	[11]

References

1. M. Wu, X. Wang, F. Zhang, Q. Xiang, Y. Li and J. Guo, *Energy & Environmental Science*, 2024, **17**, 619-629.
2. Q. Ma, R. Gao, Y. Liu, H. Dou, Y. Zheng, T. Or, L. Yang, Q. Li, Q. Cu, R. Feng, Z. Zhang, Y. Nie, B. Ren, D. Luo, X. Wang, A. Yu and Z. Chen, *Advanced Materials*, 2022, **34**.
3. C. Chang, S. Hu, T. Li, F. Zeng, D. Wang, S. Guo, M. Xu, G. Liang, Y. Tang, H. Li, C. Han and H.-M. Cheng, *Energy & Environmental Science*, 2024, **17**, 680-694.
4. Z. Meng, Y. Jiao and P. Wu, *Angewandte Chemie International Edition*, 2023, **62**.
5. D. Wang, H. Liu, D. Lv, C. Wang, J. Yang and Y. Qian, *Advanced Materials*, 2022, **35**.
6. Z. Zhang, Y. Zhang, M. Ye, Z. Wen, Y. Tang, X. Liu and C. C. Li, *Angewandte Chemie International Edition*, 2023, **62**.
7. J. Zhang, W. Huang, L. Li, C. Chang, K. Yang, L. Gao and X. Pu, *Advanced Materials*, 2023, **35**.
8. Y. Cheng, Y. Jiao and P. Wu, *Energy & Environmental Science*, 2023, **16**, 4561-4571.
9. X. Zhang, Z. Deng, C. Xu, Y. Deng, Y. Jia, H. Luo, H. Wu, W. Cai and Y. Zhang, *Advanced Energy Materials*, 2023, **13**.
10. R. Zhao, H. Wang, H. Du, Y. Yang, Z. Gao, L. Qie and Y. Huang, *Nature Communications*, 2022, **13**.
11. D. Feng, Y. Jiao and P. Wu, *Angewandte Chemie International Edition*, 2023, **62**.